Electron Diffraction of Pyrene Nanoclusters Embedded in Superfluid Helium Droplets

Lei Lei, Yuzhong Yao, Jie Zhang, Dale Tronrud, Wei Kong, Chengzhu Zhang, Lan Xue, Léo Dontot, Mathias Rapacioli

Electron Diffraction of Pyrene Nanoclusters Embedded in Superfluid Helium Droplets

Lei Lei[1], Yuzhong Yao[1], Jie Zhang[1], Dale Tronrud[1], Wei Kong[*1]

[1]*Department of Chemistry, Oregon State University, Corvallis, OR 97331*

Chengzhu Zhang[2], Lan Xue[2]

[2]*Department of Statistics, Oregon State University, Corvallis, OR 97331*

Léo Dontot[3], and Mathias Rapacioli[3]

[3]*Laboratoire de Chimie et Physique Quantiques, LCPQ/IRSAMC, UMR5626, Université de Toulouse (UPS) and CNRS, 118 Route de Narbonne, F-31062 Toulouse, France*

Manuscript for submission to the Journal of Physical Chemistry Letters, "Clusters, Radicals, and Ions; Environmental Chemistry"

*Corresponding author, wei.kong@oregonstate.edu, 541-737-6714.

ABSTRACT:

We report electron diffraction of pyrene nanoclusters embedded in superfluid helium droplets. Using a least squares fitting procedure, we have been able to separate the contributions of helium from that of the pyrene nanoclusters, and determine the most likely structures for dimers and trimers. We confirm that pyrene dimers form a parallel double-layer structure with an interlayer distance of 3.5 Å, and suggest that pyrene trimers form a sandwich structure but the molecular planes are not completely parallel. The relative contributions of the dimers and trimers are ~6:1. This work is an extension of our effort of solving structures of biological molecules using serial single molecule electron diffraction imaging. The success of electron diffraction from an all-light-atom sample embedded in helium droplets offers reassuring evidence for the feasibility of this approach.

TOC graphics (the left is 2.58 x 1.75, and the right is 2x2):

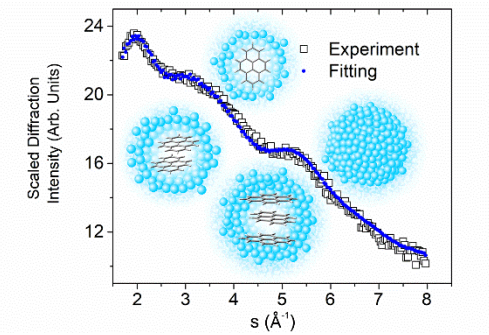

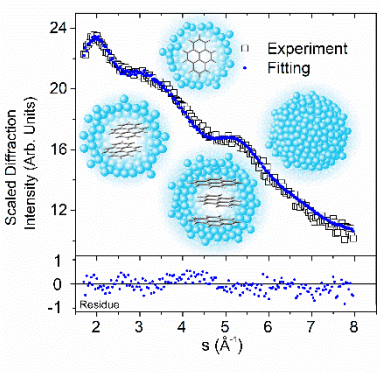

Recently, several new ideas have been introduced to solve the crystallization problem in crystallography.[1-5] One of the most successful is termed "diffract and destroy"[1] where ultrashort and ultra-intense x-ray photons are used to diffract from a single particle before the particle is destroyed by the radiation. To date, several dozens of new protein structures have already been solved using this method.[6,7] The method has been adopted to determine the shape of and detect the vortices in superfluid helium droplets.[8] Another method employs electrons because of their much larger diffraction cross sections[9] and easier accessibility in laboratories than ultra-short x-ray photons. In addition, sample alignment in a laser field prior to diffraction has also been demonstrated, simplifying the data interpretation tremendously.[2,3] The ease in aligning a molecule embedded in superfluid helium droplets has further prompted the idea of using Coulomb explosion to obtain structures of small molecules.[4,10,11]

Our group has been developing a method called serial single molecule electron diffraction imaging as a potential means to solve structures of large biological molecules and nanomaterials.[5] The procedure starts with electrospray ionization to produce ions for doping into superfluid helium droplets, and then the cooled ions are aligned by an elliptically polarized laser field and subjected to radiation by high energy electrons. The collection of images, each from molecules oriented from a chosen projection, is then used to determine the three-dimensional structure. So far we have successfully demonstrated the feasibility of doping proteins such as the green fluorescent protein into superfluid helium droplets;[12-14] and performed electron diffraction (ED) of neutral molecules including CBr_4, ferrocene, and iodine clusters embedded in superfluid helium droplets, without laser alignment.[15-17] All of these works involve molecular species that contain at least one heavy atom (with atomic

number larger than 20) to help with the contrast between the molecular diffraction and the atomic diffraction from helium. However, biological samples contain mostly carbon atoms, and the contrast issue due to similar diffraction cross sections[18] of carbon and helium has to be addressed. In this work, we expand the repertoire of our ED experiment to an all-light-atom containing species, pyrene (Py, $C_{16}H_{10}$), again without laser alignment. The goal is to demonstrate the feasibility of extracting structural information from the helium background for molecular systems that do not contain any contrasting element.

Information on pyrene clusters is limited,[19-24] with only a few theoretical efforts in the literature and no experimental result either in the gas phase nor in superfluid helium droplets. We present experimental results and detailed statistical analysis on ED of pyrene nanoclusters embedded in superfluid helium droplets. Similar to our work on iodine,[17] we observe that under our doping conditions, pyrene clusters are easily formed in the droplets. The structure of the dimer unit takes on the motif of crystalline pyrene with a similar inter-layer distance of 3.5 Å,[25-27] but the structure of the trimer is a sandwich structure with non-parallel molecular planes,[19] quite different from the crystalline structure. The presence of clusters is confirmed from time-of-flight (TOF) mass spectrometry where clusters are only observable from droplet-related pyrene and not in the diffused gaseous sample.

The experimental setup has been detailed in our previous publications.[15-17] Superfluid helium droplets are formed by supersonic expansion of high purity helium gas (99.9995%) at a stagnation pressure of 50 atm. The gas is precooled to 14 K through a closed-cycle cryostat (Sumitomo, SRDK-408SW) and expands through a nozzle of 0.05 mm in diameter (Digital Technology Trading & Marketing Ltd., E-L-5-8-C-Unmounted Cryogenic Copper Even-

Lavie valve). After passing through a skimmer of 2 mm in diameter, the droplet beam enters a doping chamber containing a sample pulsed valve (PV, Parker, series 9, 0.5 mm in nozzle diameter). Pyrene is directly loaded into the sample PV and heated to 142°C, resulting in a vapor pressure of 43 mTorr.[28] After picking up the gaseous sample, the droplet beam enters the diffraction chamber via a cone of 5 mm in diameter. To diagnose the doping condition of the droplet beam, the 4th harmonic of a pulsed Nd:YAG (Quantel, Brilliant) at 266 nm is used to ionize the embedded neutral species, at a power density of 10^6 W/cm^2 (3 mJ/pulse, 8 ns in duration, and 5 mm in beam diameter). A time-of-flight mass spectrometer perpendicular to the droplet beam resolves the ionized parent, fragment, and cluster ions. For electron diffraction, the TOF is removed and a pulsed electron beam (Kimball, physics, EGPS-6210B, 30 μs duration) at 40 keV is directed onto the droplet beam. The diffracted electrons impinge on a phosphor screen (Beam imaging Solutions, P43, 40 mm in diameter), while the undiffracted electrons are collected by a Faraday cup for beam current monitoring (1.2 mA under typical conditions). The image is recorded using an Electron Multiplying Charge Coupled Device camera (EMCCD, Andor Technology, iXon Ultra).

During the experiment, both the mass spectra and the diffraction images are recorded with active background subtraction. The sample pulsed valve containing pyrene operates at twice the repetition rate of the helium droplet beam, and the difference ($I_{diff,Py}$) between the signals obtained with ($I_{He_{on},Py}$) and without ($I_{He_{off},Py}$) the droplet beam should eliminate the contribution from gaseous pyrene diffused from the doping region into the ionization/diffraction chamber. The solenoid valve for the sample creates a magnetic field and affects the position of the electron beam, hence it has to be energized even when

recording the background. In addition, a separate diffraction profile of neat helium droplets ($I_{diff,neat}$) is recorded using the same method of active background subtraction without the sample PV after readjusting the electron gun. Unfortunately pyrene has a tendency to coat the high vacuum chamber and increase the base pressure of the doping region, from 1×10^{-7} Torr to 5×10^{-6} Torr, after a few days of operation, contaminating $I_{diff,neat}$ with embedded monomeric pyrene. The consequence of this contamination is a seemingly lower than expected concentration of monomers in the resulting net diffraction profile, while the measured concentrations of dimers and trimers are not affected. In all cases, the accumulated images recorded under all conditions are saved separately, for future data retrieval and fitting.

A major issue in diffraction of embedded samples inside helium droplets is the background of helium. For this reason, our practice has been to use the smallest droplets possible and to load as much sample as possible into the droplets.[15-17] However, limited by our visual inability to discern molecular diffraction from a strong background of monotonic decay, we ended up adopting a lower source temperature to dope more sample into each droplet. The consequence is a larger average droplet size and the presence of dopant clusters. Based on a later experiment using a retardation electrode (unpublished results), the droplet sizes at 14 K are in the range of 5×10^4 atoms/droplet.

FIG. 1 presents the TOF mass spectra of gaseous pyrene, pyrene-doped droplets, and the difference. At this laser power level (10^6 W/cm^2) and sample pressure, no fragmentation of monomers can be observed, and both the gaseous sample and the embedded sample contain monomeric parent ions. However, only doped droplets contain Py_n^+ (n = 2 to 4). We note that the presence of pyrene clusters should only be treated as evidence of existence, since the

degree of fragmentation after ejection from the doped droplet is unknown. The energy of two photons at 266 nm (total energy: 9.3 eV) is more than sufficient to both ionize[29,30] and dissociate (or dissociate and ionize) a pyrene dimer to produce $Py^+ + Py$.[19,21,31]

Fig. 2 shows the scaled radial profiles of the experimental diffraction patterns obtained after 232559 shots (12.92 Hours at a repetition rate of 5 Hz), and the inset shows the unscaled radial distribution from the raw experimental data. After a scaling factor of 7.5 for the doped droplet, no difference can be seen between the doped and neat droplets on the linear scale. To contrast the difference between the two results, the radial profiles are scaled by s^2, where s is the momentum transfer defined as:[9]

$$s = \frac{4\pi}{\lambda}\sin\left(\frac{\theta_d}{2}\right) \quad (1)$$

in terms of the de Broglie wavelength λ (0.06 Å at 40 keV) and the diffraction angle θ_d. The predominant monotonic decay is due to atomic scattering, including He, C, and H, while only coherent diffraction from atomic pairs produces constructive and destructive interferences.

To derive structural information from the diffraction profile, contributions from the helium background and from all possible pyrene clusters need to be included. Fig. 3 shows the theoretical diffraction profiles of pyrene clusters based on a few theoretical calculations and some representative cuts from crystalline pyrene.[19-27] The crystal structure and designations of molecular axes are shown in the inset of panel (a). In diffraction, shorter interatomic pairs such as the C-C bonds are manifested as longer-wavelength (in terms of s) oscillations, hence the profiles of the monomer and all clusters are similar in the region with $s \geq 5$ Å^{-1}, and the differences are primarily in the region with $s < 5$ Å^{-1}. From panels (a) to (c), with increasing

cluster sizes, the diffraction profiles demonstrate more subtle features and increases in overall intensity.

Several theoretical calculations on the structures of pyrene clusters have been reported in the literature.[19-21] The most recent is by Dontot, Spiegelman, and Rapacioli (DSR), reporting a rotation angle of 67° but a slightly non-parallel arrangement between the two molecular planes.[19] However, the authors reported a shallow minimum, with 4 other structures competitive within 20 meV: they all have parallel molecular planes but shifted or rotated by different angles as shown in the inset of Fig. 3(b). The structure labeled SPL is the global minimum by Gonzales and Lim,[20] and it involves a parallel slip between the two monomers along the long axis and an interplanar distance of 3.51 Å, in agreement with the distance in the dimeric unit of crystals.[25-27] The other three parallel dimers include SPS – slip along the short axis, GR – slip along a C-C bond, and cross – a rotation of 90°.[21] All 4 structures have very similar diffraction profiles, and hence are referred to as the *Para*-dimer in the following discussion. The trimer structure from the DSR calculation is stacked but slightly non-paralllel, quite different from a trimeric cut of crystalline pyrene, while the tetramer structure is a 3+1 construct, with the 4th pyrene nearly perpendicular to the stacked trimer.[19]

An earlier report by Takeuchi (HT structure) contains a parallel dimer,[24] a parallel trimer, and a near-cyclic tetramer. The HT dimer, although slightly different from the 4 parallel dimers, has a very similar diffraction profile to those of the parallel dimers.

Other possible structures include different cuts from the crystalline structure. Crystalline pyrene consists of dimeric units,[25-27] so the 3rd pyrene in a trimer should belong to a nearby dimer, and it should be nearly perpendicular (tightly packed) to the central dimer from a

stability point of view. Similarly, pyrene tetramer should contain two dimers packed nearly perpendicular to each other. We have also considered larger clusters based on a variety of cut-outs of crystalline structures,[25-27] but statistical analysis of both the fitting result and doping probability indicates that contributions from clusters larger than tetramers are negligible.

Mixtures of the different sets of structures, for example, a parallel dimer and a DSR trimer, are also possible. However, if we include all possible cluster structures, 3 for dimer (DSR, HT, and Para), 3 for trimer, and 3 for tetramer (DSR, HT, and crystal cutout), for a global fit, we would have 11 independent parameters (in addition to β and α_0). To alleviate model complexity, we chose to fit 4 sets of structures independently, including the DSR and the HT set, a mix_P set containing the parallel dimer and the DSR trimer, and a mix_T set containing the HT dimer and the DSR trimer. The structures of trimers and tetramers derived from crystalline pyrene are eliminated because when added to any one of the sets, the resulting coefficients for these structures are essentially zero.

To compare the relative quality of the different models in fitting the experimental data, we used the Akaike information criterion (AIC) defined as

$$AIC = m \cdot ln(\hat{\sigma}^2) + 2k, \tag{5}$$

where m is the number of data points (sample size), $\hat{\sigma}^2$ is the Sum of Squared Residuals (SSR) over m, and k is the number of fitting parameters.[32] Models are considered equivalent when their AIC difference is ≤ 2,[33] while a model is strongly preferred when its AIC is lower by more than 10 than the AICs of other models.

In performing the least squares fitting procedure, the resemblance of the diffraction profiles

from different clusters – all containing the contribution of monomers – creates a numerical challenge. We remove the dependency by subtracting the contributions of monomers (I_1) from the theoretical profiles of the cluster containing n monomers (I_n) and use I_{n_C} for each cluster:

$$I_{n_C} = I_n - n \cdot I_1, \tag{2}$$

to fit only the un-correlated components of each cluster. The resulting model is therefore:

$$I_{diff,Py} = \beta \cdot I_{diff,neat} + \alpha_0 + \alpha_1 \cdot I_1 + \sum \alpha_{2_i} \cdot I_{2Ci} + \sum \alpha_{3_i} \cdot I_{3Ci} + \sum \alpha_{4_i} \cdot I_{4Ci}\,. \tag{3}$$

The coefficients α and β are fitting parameters related to the contribution of each component in the overall diffraction profile, and α_0 is a baseline correction largely due to leaked light into the camera. The value of β represents the contribution of the remaining helium after doping relative to that of a neat droplet beam. The values of α_{n_i} (n > 1) represent contributions of clusters containing n monomers with structure i, but the net contribution of pyrene monomers $\alpha_{monomer}$ is:

$$\alpha_{monomer} = \alpha_1 - 2 \cdot \sum \alpha_{2_i} - 3 \cdot \sum \alpha_{3_i} - 4 \cdot \sum \alpha_{4_i}\,. \tag{4}$$

Evaluation of the fitting results follows a few principles. Two constraints are implemented in the fitting, including that all parameters α_n (n > 1) being non-negative, and that $\alpha_{monomer} \geq 0$. Although not implemented in the fitting, we also use Poisson doping statistics and the mass spectrum in Fig. 1 to validate the distribution of the resulting coefficients.[34]

Table I lists the resulting SSR and AIC values for the 4 sets of models. Model 1 considers the possibility of only monomers in the droplets, and it is independent of cluster structures. Subsequent models are numbered by the largest size of clusters in the model with the

structures labeled by subscripts. The most likely model with the lowest AIC value, 3_{mix_P} (highlighted in bold-face), contains the parallel dimer and the DSR trimer. The model 4_{mix_P} has the second lowest AIC value, but the fitted coefficient $\alpha_{4_{DSR}}$ is zero, and the increase in its AIC is a result of the increased number of parameters. Based on Table I, there is essentially no support for the next level of models containing only dimers with the parallel (2_{mix_P}) or the HT (2_{mix_T}) structure, or model 3_{HT}.[33]

To confirm the significance of the regression coefficients, we used the bootstrap resampling method through balanced variable selection to determine the standard error of each estimate.[35] The resulting *Z* values, i.e. the ratio of the estimated coefficient and its standard error, are compared with a critical value (1.28) from a standard Normal distribution for a chosen significant level (0.1). Table II shows the resulting fitting coefficients and their ratios, uncertainties, and the corresponding *Z* values.

Figure 4 compares the experimental data with the fitting results, and the residue is shown in the bottom panel. Similar to Fig. 2, both the radial profiles and the residues are scaled with s^2. The two experimental values $I_{diff,Py}$ and $I_{diff,neat}$ were recorded with the same exposure time, and the small value of β signifies that more than 90% of the helium atoms could not reach the diffraction region. This level of elimination is on par with our previous work on ferrocene and iodine.[16,17] The effective high vapor pressure in the doping region destroys most of the small droplets with or without a dopant monomer.

To further understand the contribution of Py_n in the diffraction pattern, we model the doping process using Poisson statistics. We estimate the number of evaporated helium atoms (2000) upon cooling a pyrene molecule from 142°C to 0.4 K based on the heat capacity of solid

pyrene (229 J/K·mol)[28] and the binding energy of helium (0.6 meV).[36,37] After the first collision, 4% of the helium atoms is lost in a droplet of 5×10^4 atoms/droplet. This size change is negligible and standard Poisson distribution can be used to calculate the probability of doping.[34] Based on the empirical formula of supersonic expansion,[38] the pressure in the doping region 7 mm away from the sample nozzle of 0.5 mm should be 1.3×10^{-5} Torr. With a doping distance of 7 mm, the probability of doping 0 – 4 pyrene is 0.71:0.24:0.04:0.004:0.0005 (the ratios of the corresponding α_i values are listed in the last column of Table II). The relative abundance of Py_2 and Py_3 is in qualitative agreement with that from the fitting. The much larger contribution of monomers from the doping statistics than that from fitting of the diffraction pattern is attributed to contamination in the neat droplet diffraction profile $I_{diff,neat}$.

The doping statistics and the fitting results of the diffraction profile are on par with the abundance of Py_n^+ in the mass spectra of Fig. 1. We have limited information on the ionization mechanism of Py_n^+. However, we speculate that the abundant Py^+ is most likely a result of dissociation of Py_n or Py_n^+ after desorption from the droplet. The missing contribution from Py_4 in the diffraction profile should be a result of low concentration.

In conclusion, the diffraction profile from this experiment of pyrene doped droplets contains mostly contributions from Py_1 and Py_2, with indications of a ~10% contribution from Py_3. The structure of Py_2 contains two parallel pyrene molecules, and that of Py_3 appears to be stacked but not completely parallel. This structure of Py_3, in our best fitting model, is different from that of the crystalline structure, demonstrating that at least in superfluid helium droplets, the stacking force prevails against the tendency of forming a 3-D closely packed

structure. Different from our previous work, pyrene contains no heavy atoms, and the success of this work offers promise in obtaining molecular parameters from all-light-atom containing species in superfluid helium droplets. The contrast issue, arising from the small difference in diffraction cross sections of light atoms (carbon in particular) and helium, is shown to be solvable. With proper statistical treatment, we can not only identify the most likely structures of pyrene dimers and trimer, but also have a reasonable estimate on the abundance of each sized cluster.

ACKNOWLEDGEMENTS

This material is based upon work supported by National Institute of General Medical Sciences (1R01GM101392-01A1) from the National Institutes of Health.

REFERENCE

(1) Neutze, R.; Wouts, R.; van, d. S. D.; Weckert, E.; Hajdu, J. Potential for Biomolecular Imaging with Femtosecond X-Ray Pulses, *Nature* **2000**, *406*, 752-757.

(2) Yang, J.; Centurion, M. Gas-Phase Electron Diffraction from Laser-Aligned Molecules, *Struct. Chem.* **2015**, *26*, 1513-1520.

(3) Karamatskos, E. T.; Mullins, T.; Trabattoni, A.; Dlugolecki, K.; Trippel, S.; Kupper, J.; Karamatskos, E. T.; Trabattoni, A.; Kupper, J.; Raabe, S.; Stammer, P.; Goldsztejn, G.; Vrakking, M. J. J.; Rouzee, A.; Johansen, R. R.; Stapelfeldt, H.; Trippel, S.; Kupper, J. Molecular Movie of Ultrafast Coherent Rotational Dynamics of Ocs, *Nat Commun* **2019**, *10*, 3364.

(4) Schouder, C.; Chatterley, A. S.; Calvo, F.; Christiansen, L.; Stapelfeldt, H. Structure Determination of the Tetracene Dimer in Helium Nanodroplets Using Femtosecond Strong-Field Ionization, *Struct. Dyn.* **2019**, *6*, 044301.

(5) Beckman, J.; Kong, W.; Voinov, V. G.; Freund, W. M., USA Patent No. US20150168318A1 (March 8, 2016).

(6) Johansson, L. C.; Stauch, B.; Ishchenko, A.; Cherezov, V. A Bright Future for Serial Femtosecond Crystallography with Xfels, *Trends Biochem. Sci.* **2017**, *42*, 749-762.

(7) Neutze, R. Opportunities and Challenges for Time-Resolved Studies of Protein Structural Dynamics at X-Ray Free-Electron Lasers, *Philos. Trans. R. Soc. Lond. B Biol Sci.* **2014**, *369*, 20130318.

(8) Gessner, O.; Vilesov, A. F. Imaging Quantum Vortices in Superfluid Helium Droplets, *Annu. Rev. Phys. Chem.* **2019**, *70*, 173-198.

(9) Brockway, L. O. Electron Diffraction by Gas Molecules, *Rev. Mod. Phys.* **1936**, *8*, 231-266.

(10) Pickering, J. D.; Shepperson, B.; Hubschmann, B. A. K.; Thorning, F.; Stapelfeldt, H. Alignment and Imaging of the Cs2 Dimer inside Helium Nanodroplets, *Phys. Rev. Lett.* **2018**, *120*, 113202.

(11) Pickering, J. D.; Shepperson, B.; Christiansen, L.; Stapelfeldt, H. Femtosecond Laser Induced Coulomb Explosion Imaging of Aligned Ocs Oligomers inside Helium Nanodroplets, *J. Chem. Phys.* **2018**, *149*, 154306.

(12) Zhang, J.; Chen, L.; Freund, W. M.; Kong, W. Effective Doping of Low Energy Ions into Superfluid Helium Droplets, *J. Chem. Phys.* **2015**, *143*, 074201.

(13) Chen, L.; Zhang, J.; Freund, W. M.; Kong, W. Effect of Kinetic Energy on the Doping Efficiency of Cesium Cations into Superfluid Helium Droplets, *J. Chem. Phys.* **2015**,

143, 044310.

(14) Alghamdi, M.; Zhang, J.; Oswalt, A.; Porter, J. J.; Mehl, R. A.; Kong, W. Doping of Green Fluorescent Protein into Superfluid Helium Droplets: Size and Velocity of Doped Droplets, *J. Phys. Chem. A* **2017**, *121*, 6671-6678.

(15) He, Y.; Zhang, J.; Kong, W. Electron Diffraction of Cbr_4 in Superfluid Helium Droplets: A Step Towards Single Molecule Diffraction, *J. Chem. Phys.* **2016**, *145*, 034307.

(16) Zhang, J.; He, Y.; Kong, W. Communication: Electron Diffraction of Ferrocene in Superfluid Helium Droplets, *J. Chem. Phys.* **2016**, *144*, 221101.

(17) He, Y.; Zhang, J.; Lei, L.; Kong, W. Self-Assembly of Iodine in Superfluid Helium Droplets: Halogen Bonds and Nanocrystals, *Angew. Chem., Int. Ed.* **2017**, *56*, 3541-3545.

(18) Jablonski, A. S., F.; Powell, C. J. *Nist Electron Elastic-Scattering Cross-Section, Database, Version 3.2, Srd 64*; National Institute of Standards and Technology: Gaithersburg, MD, 2010.

(19) Dontot, L.; Spiegelman, F.; Rapacioli, M. Structures and Energetics of Neutral and Cationic Pyrene Clusters, *J. Phys. Chem. A* **2019**, *123*, 9531-9543.

(20) Gonzalez, C.; Lim, E. C. Evaluation of the Hartree-Fock Dispersion (Hfd) Model as a Practical Tool for Probing Intermolecular Potentials of Small Aromatic Clusters: Comparison of the Hfd and Mp2 Intermolecular Potentials, *J. Phys. Chem. A* **2003**, *107*, 10105-10110.

(21) Podeszwa, R.; Szalewicz, K. Physical Origins of Interactions in Dimers of Polycyclic Aromatic Hydrocarbons, *Phys. Chem. Chem. Phys.* **2008**, *10*, 2735-2746.

(22) Rapacioli, M.; Calvo, F.; Spiegelman, F.; Joblin, C.; Wales, D. J. Stacked Clusters of Polycyclic Aromatic Hydrocarbon Molecules, *J. Phys. Chem. A* **2005**, *109*, 2487-2497.

(23) Rapacioli, M.; Spiegelman, F.; Talbi, D.; Mineva, T.; Goursot, A.; Heine, T.; Seifert, G. Correction for Dispersion and Coulombic Interactions in Molecular Clusters with Density Functional Derived Methods: Application to Polycyclic Aromatic Hydrocarbon Clusters, *J. Chem. Phys.* **2009**, *130*, 244304.

(24) Takeuchi, H. Structures, Stability, and Growth Sequence Patterns of Small Homoclusters of Naphthalene, Anthracene, Phenanthrene, Phenalene, Naphthacene, and Pyrene, *Comput. Theor. Chem.* **2013**, *1021*, 84-90.

(25) Frampton, C. S.; Knight, K. S.; Shankland, N.; Shankland, K. Single-Crystal X-Ray Diffraction Analysis of Pyrene Ii at 93 K, *J. Mol. Struct.* **2000**, *520*, 29-32.

(26) Robertson, J. M.; White, J. G. The Crystal Structure of Pyrene. A Quantitative X-Ray Investigation, *J. Chem. Soc.* **1947**, 358-368.

(27) Hazell, A. C.; Larsen, F. K.; Lehmann, M. S. Neutron Diffraction Study of the Crystal Structure of Pyrene, C16h10, *Acta Crystallogr., Sect. B* **1972**, *28*, 2977-2984.

(28) Smith, N. K.; Stewart, R. C., Jr.; Osborn, A. G.; Scott, D. W. Pyrene: Vapor Pressure, Enthalpy of Combustion, and Chemical Thermodynamic Properties, *J. Chem. Thermodyn.* **1980**, *12*, 919-926.

(29) Khan, Z. H. Electronic Spectra of Radical Cations and Their Correlation with Photoelectron Spectra. Vi. A Reinvestigation of Two-, Three-, and Four-Ring Condensed Aromatics, *Acta Phys. Pol., A* **1992**, *82*, 937-955.

(30) Joblin, C.; Dontot, L.; Garcia, G. A.; Spiegelman, F.; Rapacioli, M.; Nahon, L.; Parneix, P.; Pino, T.; Bréchignac, P. Size Effect in the Ionization Energy of Pah Clusters, *J. Phys. Chem. Lett.* **2017**, *8*, 3697-3702.

(31) Schuetz, C. A.; Frenklach, M. Nucleation of Soot: Molecular Dynamics Simulations of Pyrene Dimerization, *Proc. Combust. Inst.* **2002**, *29*, 2307-2314.

(32) Akaike, H. A New Look at the Statistical Model Identification, *IEEE Trans. Autom. Control* **1974**, *19*, 716-723.

(33) Burnham, K. P.; Anderson, D. R. Multimodel Inference: Understanding Aic and Bic in Model Selection, *Sociol. Methods Res* **2004**, *33*, 261-304.

(34) Hartmann, M.; Miller, R. E.; Toennies, J. P.; Vilesov, A. F. High-Resolution Molecular Spectroscopy of Van Der Waals Clusters in Liquid Helium Droplets, *Science* **1996**, *272*, 1631-1634.

(35) Efron, B. Bootstrap Methods: Another Look at the Jackknife, *Ann. Statist.* **1979**, *7*, 1-26.

(36) Toennies, J. P. Helium Clusters and Droplets: Microscopic Superfluidity and Other Quantum Effects†, *Mol. Phys.* **2013**, *111*, 1879-1891.

(37) Slenczka, A.; Toennies, J. P. Chemical Dynamics inside Superfluid Helium Nanodroplets at 0.37 K. In *Low Temperatures and Cold Molecules*; Smith, I. W. M., eds.; World Scientific Press: Singapore, 2008, pp. 345-392.

(38) Miller, D. R. Free Jet Sources. In *Atomic and Molecular Beam Methods*; Scoles, G., eds.; Oxford University Press: New York, 1988; Vol. I, pp. 14-53.

Table I. Comparisons of fitting results from different sets of structures and models.

Model #	Cluster fitting formula*	SSR	AIC
1	$(monomer\ only)$	0.668	-1055
2_{mix_P}	$\alpha_{2_{Para}} \cdot I_{2_{Para}}$	0.143	-1352
3_{mix_P}	$\boldsymbol{\alpha_{2_{Para}} \cdot I_{2_{Para}} + \alpha_{3_{DSR}} \cdot I_{3_{DSR}}}$	**0.121**	**-1380**
4_{mix_P}	$\alpha_{2_{Para}} \cdot I_{2_{Para}} + \alpha_{3_{DSR}} \cdot I_{3_{DSR}} + \alpha_{4_{DSR}} \cdot I_{4_{DSR}}$	0.121	-1378[a]
2_{mix_T}	$\alpha_{2_{HT}} \cdot I_{2_{HT}}$	0.140	-1354
3_{mix_T}	$\alpha_{2_{HT}} \cdot I_{2_{HT}} + \alpha_{3_{DSR}} \cdot I_{3_{DSR}}$	0.140	-1352[a]
4_{mix_T}	$\alpha_{2_{HT}} \cdot I_{2_{HT}} + \alpha_{3_{DSR}} \cdot I_{3_{DSR}} + \alpha_{4_{DSR}} \cdot I_{4_{DSR}}$	0.140	-1350[a]
2_{DSR}	$\alpha_{2_{DSR}} \cdot I_{2_{DSR}}$	0.157	-1333
3_{DSR}	$\alpha_{2_{DSR}} \cdot I_{2_{DSR}} + \alpha_{3_{DSR}} \cdot I_{3_{DSR}}$	0.153	-1335[a]
4_{DSR}	$\alpha_{2_{DSR}} \cdot I_{2_{DSR}} + \alpha_{3_{DSR}} \cdot I_{3_{DSR}} + \alpha_{4_{DSR}} \cdot I_{4_{DSR}}$	0.150	-1337[a]
3_{HT}	$\alpha_{2_{HT}} \cdot I_{2_{HT}} + \alpha_{3_{HT}} \cdot I_{3_{HT}}$	0.140	-1352[a]
4_{HT}	$\alpha_{2_{HT}} \cdot I_{2_{HT}} + \alpha_{3_{HT}} \cdot I_{3_{HT}} + \alpha_{4_{HT}} \cdot I_{4_{HT}}$	0.140	-1350[a]

*The total formula also includes $\beta \cdot I_{diff,neat} + \alpha_0 + \alpha_1 \cdot I_1$.

[a]The coefficient for the last term (largest cluster) is more than 3 orders of magnitude smaller than the previous term (next largest cluster).

Table II. Constrained least squares fitting result of embedded Py_n (n = 1 – 3) in superfluid helium droplets from the best model 3_{mix_P}.

Term	Coefficient	Standard error	Z	Coefficient Ratio	Ratio from Doping
β	0.06194	0.00054	114.7		
$\square_0$	0.01210	0.00170	7.11		
$\square_1$	0.00798	0.00069	11.5	18	99
$\alpha_{2_{Para}}$	0.00262	0.00072	3.62	6	8
$\alpha_{3_{DSR}}$	0.00044	0.00030	1.45	1	1

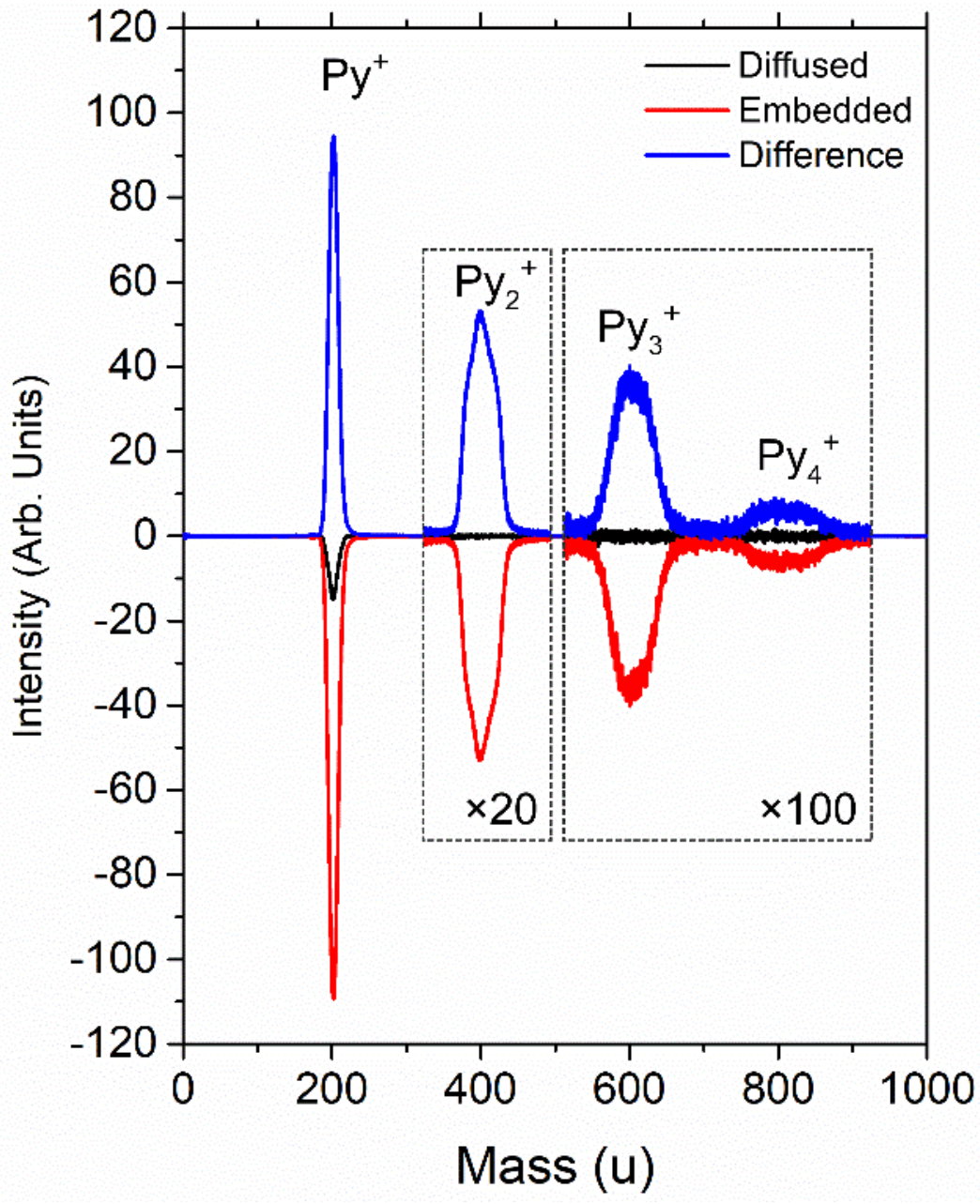

FIG. 1. TOF mass spectra of pyrene related species.

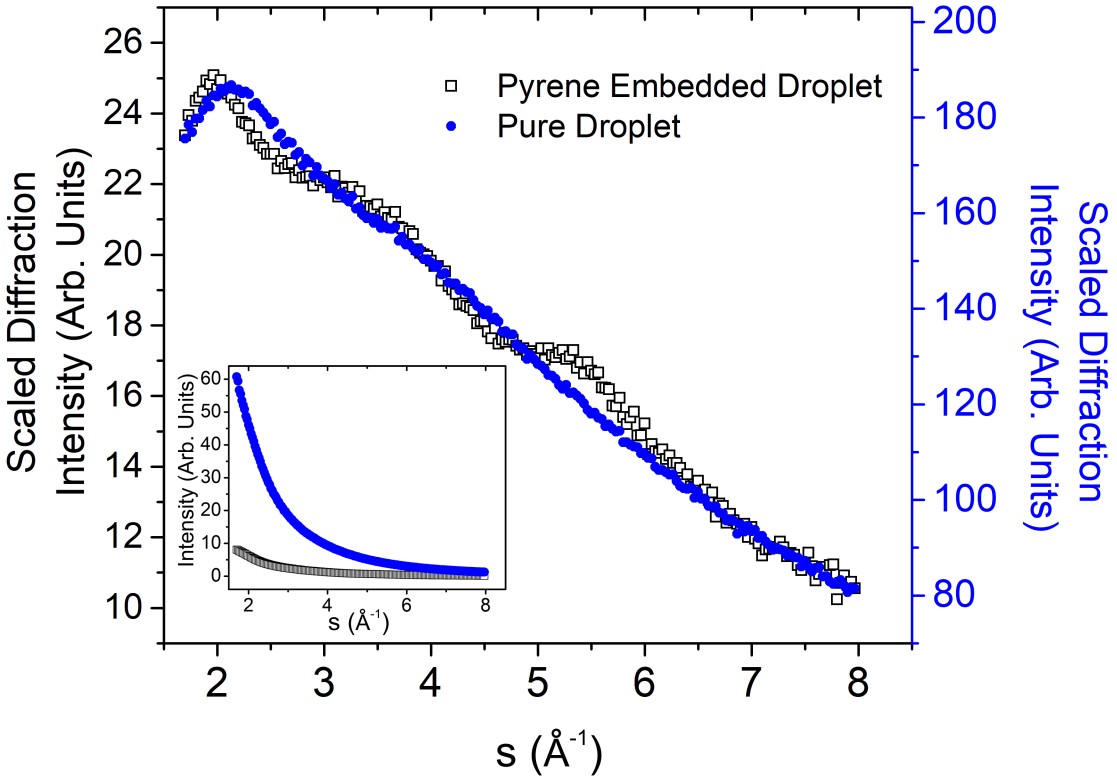

FIG. 2. Radial profiles of diffraction patterns from neat and pyrene doped droplets. The inset shows the relative intensities of the radial profiles. With a multiplication factor of 7.5, the two profiles in the inset overlap exactly. By multiplying the profiles with s^2, the difference between the doped and neat droplets can be seen in the scaled plot.

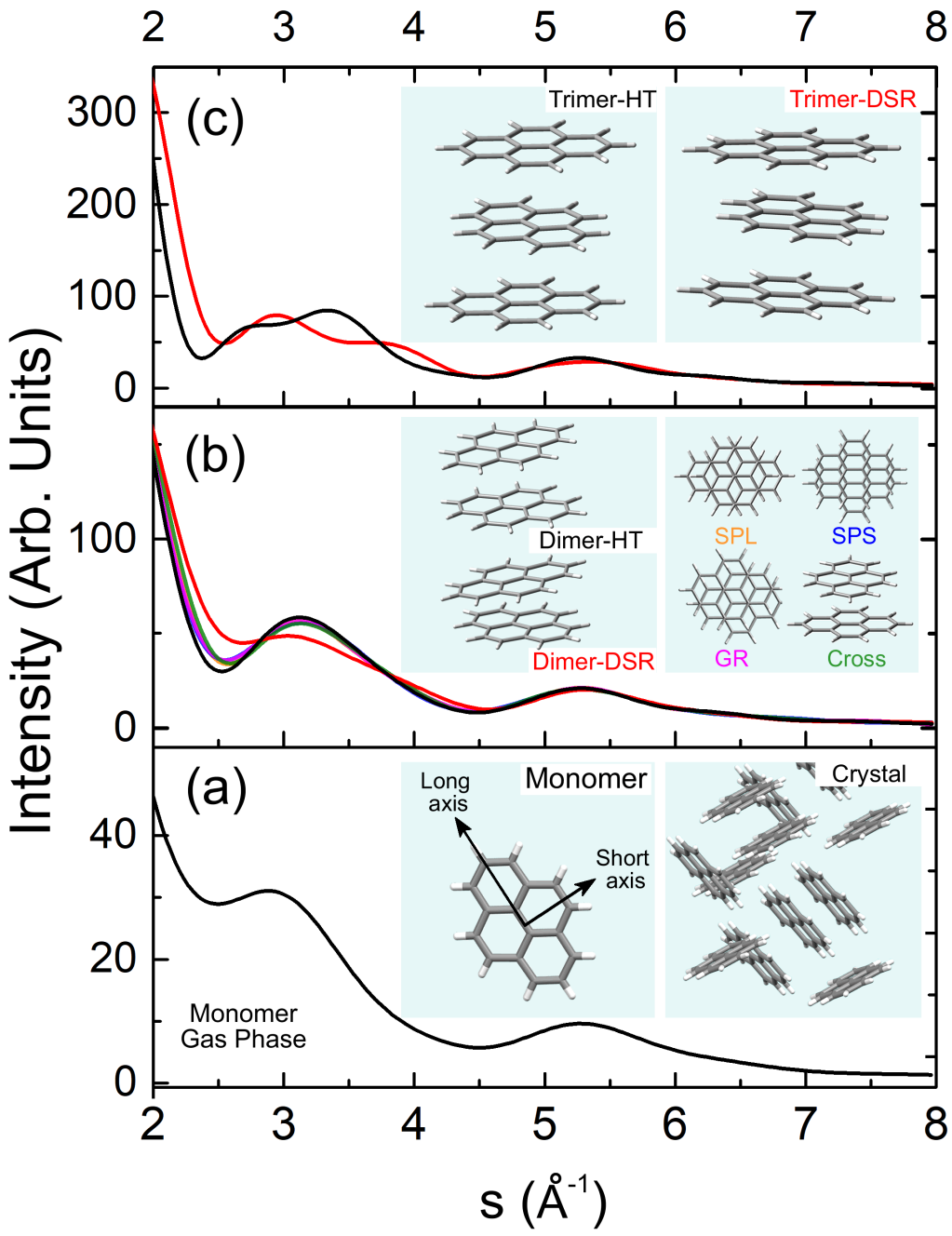

FIG. 3. Theoretical diffraction profiles from selected structures of pyrene clusters. The diffraction profile of each structure is color-coded within each panel. The diffraction profile in Panel (a) is from the monomer.

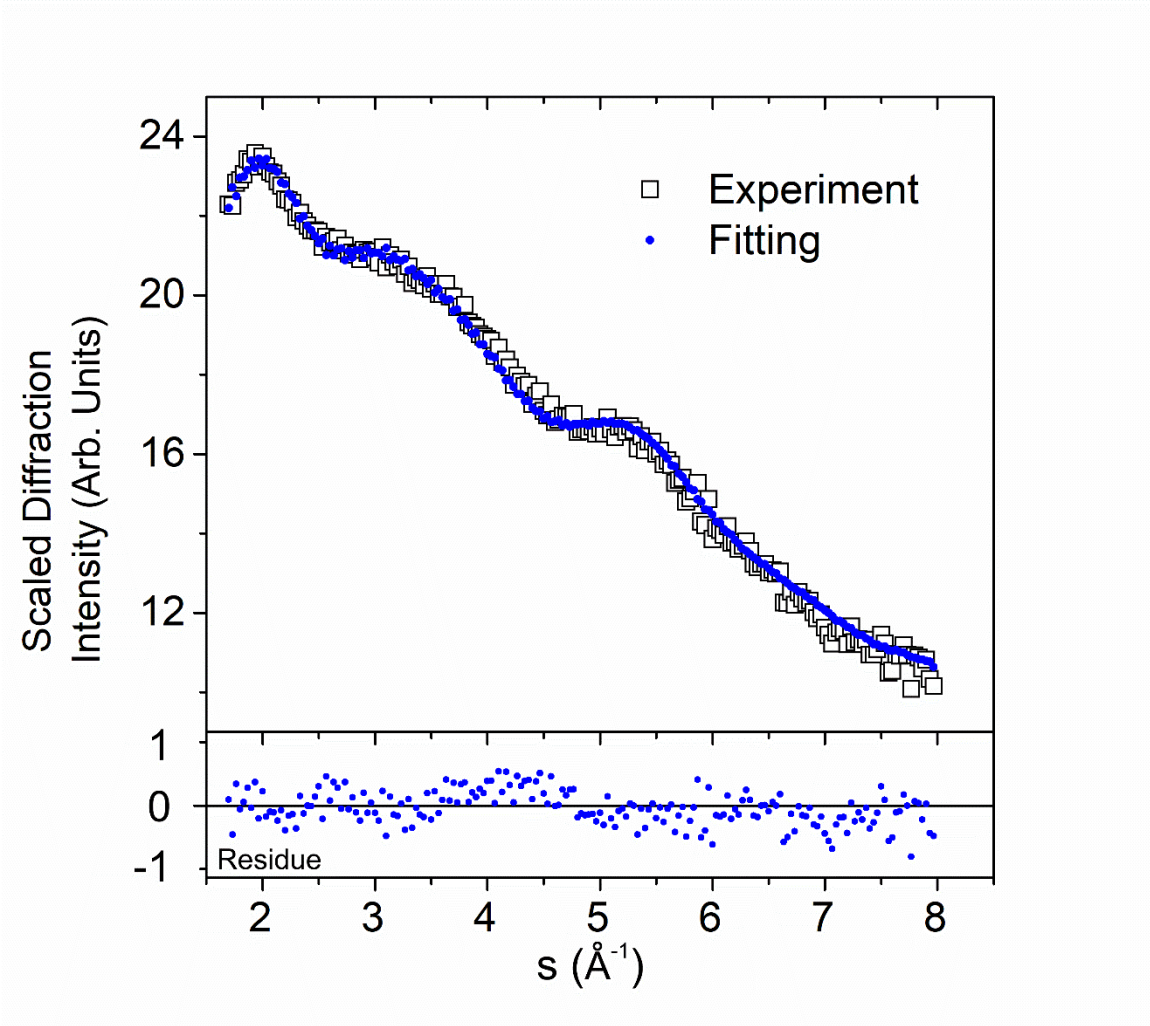

Fig. 4. Comparison of scaled experimental and fitting results. The residue is the difference between the scaled radial profiles.